

## Numerical Analysis of Crack-Tip Fields using a Meshless Method in Linear Elastic Materials

Zahra Sheikhi<sup>1</sup>, Akbar Ghanbari<sup>2,\*</sup>, Mohammad Karkon<sup>2</sup>  
and Soleyman Ghouhestani<sup>3</sup>

<sup>1</sup> Department of Civil Engineering, Larestan Branch, Islamic Azad University, Larestan, Iran

<sup>2</sup> Department of Civil Engineering, Larestan Branch, Islamic Azad University, Larestan, Iran

<sup>3</sup> Department of Civil Engineering, Fasa University, Fasa, Iran

Received 28 February 2021; Accepted (in revised version) 18 September 2021

---

**Abstract.** In this paper, the Discrete Least Squares Meshless (DLSM) method is developed to determine crack-tip fields. In DLSM, the problem domain and its boundary are discretized by unrelated field nodes used to introduce the shape functions by the moving least-squares (MLS) interpolant. This method aims to minimize the sum of squared residuals of the governing differential equations at any nodal point. Since high-continuity shape functions are used, some necessary treatments, including the visibility criterion, diffraction, and transparency approaches, are employed in the DLSM to introduce strong discontinuities such as cracks. The stress extrapolation and  $J$ -integral methods are used to calculate stress intensity factors. Three classic numerical examples using three approaches to defining discontinuities in the irregular distribution of nodal points are considered to investigate the effectiveness of the DLSM method. The numerical tests indicated that the proposed method effectively employed the approaches to defining discontinuities to deal with discontinuous boundaries. It was also demonstrated that the diffraction approach obtained higher accuracy than the other techniques.

**AMS subject classifications:** 74A45, 65N22, 74S99

**Key words:** Numerical analysis, partial differential equations, fracture mechanics, meshless method, discrete least-squares, modification of weight function, approaches to defining discontinuities, stress intensity factors.

---

\*Corresponding author.

Emails: zahra\_sheikhii@yahoo.com (Z. Sheikhi), akbar\_ghanbarii@yahoo.com (A. Ghanbari), karkon1442@gmail.com (M. Karkon), s.ghouhestani@gmail.com (S. Ghouhestani)

## 1 Introduction

Structural defects such as micro-cracks always have an adverse effect on their service life. Therefore, it is essential to investigate crack-tip fields to determine the safety factors and predict the service life of mechanical structures. Recent years have seen substantial growth in the use of fracture mechanics in structural analysis and design. Crack problems can be analyzed as elliptic partial differential equations (PDEs) whereby crack-tip stress singularities can be explained, which is determined by the stress intensity factor (SIF).

Analytical solutions can be used to solve crack problems with regular, non-complex boundaries in infinite planes. However, numerical methods must be applied to solve various fracture mechanics problems with complex geometric configurations and loading conditions. The finite element method (FEM) is employed as usual to solve fracture mechanics problems. The domain meshing-based methods, e.g., FEM, have some shortcomings in calculating fracture mechanic parameters, including failure to accurately identify near-crack-tip singularities [1] and limited ability to model the crack growth. The FEM requires mesh modification and updating to simulate the crack growth, a time-consuming and costly process. The boundary element method (BEM) [2] was applied to solve crack problems, as it is a time-efficient, sufficiently accurate method that only requires boundary discretization. The extended finite element method (XFEM) [3] is an improved version of the FEM that is appropriately designed for fracture mechanics problems [4]. The XFEM has certain advantages over the conventional FEM; for example, it can model cracks with arbitrary geometric shapes independently of the FEM meshes, and it requires minimal re-meshing in solving crack growth problems. Although some methods, e.g., node release, are introduced to overcome the existing problems [5,6], some challenges still exist.

The problems detailed above and other shortcomings such as strain/stress discontinuity on element surfaces and the need for some additional operations for smoothing the results have motivated researchers to try other numerical methods [1]. Thus, several meshless methods are introduced to overcome these problems. Meshless methods are developed under two branches of formulations: weak form and strong form. The problem domain is discretized using nodal points in both methods. However, weak-form meshless methods require background meshes to obtain Gauss points for integration despite the higher relative accuracy of the results. In some cases, these meshless methods incur a higher computational cost than mesh-based methods, where integration problems at complex boundaries still persist. Strong-form meshless methods, on the other hand, directly solve PDEs and reduce the computational cost. However, they have certain disadvantages, such as instability, low accuracy of the results, difficulty in applying boundary conditions, and asymmetric coefficient matrix.

The application of smooth interpolants in meshless methods has led to the desired results, rendering them advantageous over the FEM. Besides, they have outperformed the FEM in solving problems with moving boundaries, large deformation, and crack propagation. Despite these advantages, meshless methods also have some disadvantages, in-

cluding the use of complex, high-continuity shape functions, difficulty in the fulfillment of boundary conditions, and the required corrections in the simulation of discontinuities. However, different techniques have been proposed in meshless methods to implement discontinuities. Among them, four approaches are generally proposed to introduce discontinuity in meshless methods [7]. The first scheme is based on the modification of weight functions; visibility criterion, diffraction, and transparency approaches [8,9] fall into this category. The second scheme includes modification of the intrinsic basis [10] to consider special functions. The third scheme consists of enriched methods based on MLS shape functions [10]. In the fourth scheme, the enriched partition of unity method (PUM) [11,12] is used to deal with discontinuities. Moreover, some research [13,14] has recently applied the augmented Lagrangian method to model crack problems containing material discontinuities as strong and weak discontinuities. Each of these techniques has its own complexities.

The visibility criterion, diffraction, and transparency approaches are the most popular meshless methods for modeling discontinuities [15]. Belytschko et al. [16] developed the visibility criterion to incorporate crack problems into meshless methods. Organ et al. [9] applied the diffraction approach, i.e., an extension of the visibility criterion, for nonconvex boundaries such as a crack in the element-free Galerkin (EFG) method. They proposed the transparency approach as superseded by the diffraction approach in three-dimensional (3D) problems. Other meshless methods attempted to modify the weight function using the three techniques detailed above or in combination with other techniques for simulating crack problems. Muravin and Turkel [17] proposed the spiral weight method, which was an improvement to the diffraction approach to come up with a more accurate solution to arbitrary crack problems. Pirali et al. [18] simulated crack discontinuities in the EFG method using a combined node searching algorithm called combined visibility and surrounding triangles (CVT). In this approach, the nodes located on the crack faces employed the visibility criterion. The surrounding triangles method generated by quadrature points was applied to the influence domain of master nodes near the crack faces. Khezri et al. [19] presented a coupling of the finite strip method (FSM) and the reproducing kernel particle method (RKPM) to analyze the two-dimensional (2D) elastic problem domain containing cracks using the visibility criterion for defining discontinuities. In [20], the EFG method was enriched with two-level nesting triangular sub-domains (NSEMM). In this study, strong discontinuities are defined using the diffraction approach, and an enriched MLS interpolant was employed to construct the near-crack-tip shape functions. The generalized finite difference method (GFDM) was applied by Lei et al. [21] to solve static plane crack problems using a scheme based on the visibility criterion. In this scheme, in the vicinity of the crack tip, the nodes excluded from the support domain in the visibility criterion approach were replaced in the visible area. Yao et al. [22] simulated nonconvex boundaries with a focus on the crack in the continuous smoothed particle hydrodynamics (CSPH) method using the diffraction approach.

Recently, the least-squares method (LSM) has been widely applied to solve PDEs. Af-

shar and Arzani [23] proposed a novel LSM-derived method called the discrete least-squares meshless (DLSM) method to provide a solution to Poisson's equation. This method has been successfully adopted to solve elliptic PDEs [24], as well as fluid mechanics [25–28] and elasticity [29–34] problems, alone or in conjunction with other numerical methods. In this approach, the solution domain is discretized by nodes employed for constructing the shape functions using the MLS interpolant. This is a truly meshless method since it does not require any background cells for problem-solving. This method minimizes the least-squares functional defined as the weighted sum of squared residuals of the governing equations and its natural and essential boundary conditions at any nodal point. It employed the LSM to discretize the governing equations and interpolation functions since it exhibits high accuracy even in solving problems with irregular nodal distributions. The proposed method has some other advantages, including high stability, ease of application, ease of increasing or decreasing the number of nodal points, no need for any background mesh, and symmetric, banded coefficient matrix.

In this paper, the DLSM method is developed to study crack tip fields for 2D elastostatic problems in isotropic materials. For this purpose, the MLS method is initially used for constructing the shape functions, and the DLSM method is then formulated. This is followed by introducing certain treatments on the domain of influence for strong discontinuity problems based on the visibility criterion, diffraction, and transparency approaches. Afterward, linear elastic fracture mechanics (LEFM) problems, as well as the stress extrapolation and  $J$ -integral methods, are reviewed for determining SIFs. Three numerical examples are given to investigate the accuracy and efficiency of the proposed method. Finally, some concluding remarks are presented.

## 2 Approximation by Moving Least Squares (MLS) interpolation

Several studies have been carried out to approximate nodal parameters and construct shape functions, and various techniques have been developed to be applied in meshless methods. The MLS method [35] is among the best techniques used for constructing meshless shape functions due to its completeness, robustness, and continuity [36]. In the MLS technique, the unknown field value  $u(x)$  is approximated by:

$$u(x) = \sum_{i=1}^k p_i(x) a_i(x) = \mathbf{p}^T(x) \mathbf{a}(x), \quad (2.1)$$

where  $k$  is the number of polynomials in the basis vector,  $\mathbf{p}^T(x)$  is a polynomial basis generated by Pascal's pyramid for the second-order basis in the 2D domain, which can be specified as  $\mathbf{p}^T(x) = [1, x, y, x^2, xy, y^2]$ . Besides,  $\mathbf{a}(x)$  is the coefficient vector in the  $x$ -coordinate, which can be determined by minimizing the weight function as follows:

$$\mathbf{J}(x) = \sum_{j=1}^n w_j(x) \left[ \mathbf{p}^T(x_j) \mathbf{a}(x) - u^h(x_j) \right]^2, \quad (2.2)$$

where  $n$  represents the number of nodal points in the support domain,  $u^h(x_j)$  denotes the nodal parameter of the approximated function at the  $j$ th node, and  $w_j(x)$  is the weight function at point  $x$ . Meshless methods employ several weight functions to construct MLS shape functions. In this paper, a 2D cubic-spline weight function is adopted as:

$$w_j(x) = \begin{cases} \frac{2}{3} - 4\bar{r}^2 + 4\bar{r}^3, & \bar{r} \leq \frac{1}{2}, \\ \frac{4}{3} - 4\bar{r} + 4\bar{r}^2 - \frac{4}{3}\bar{r}^3, & \frac{1}{2} \leq \bar{r} \leq 1, \\ 0, & \bar{r} > 1, \end{cases} \quad (2.3)$$

where  $\bar{r} = r_j / r_{SDj}$ ,  $r_j = |x - x_j|$  and  $r_{SDj}$  is the support domain size at  $j$ th node defined as  $r_{SDj} = \gamma r_{Dk}$ , in which  $r_{Dk}$  is the distance of the  $j$ th node from the  $k$ th nearest point, and  $\gamma \geq 1$  is a constant value obtained by trial and error. By minimizing the functional  $J(x)$  in Eq. (2.2) relative to the vector of coefficients  $\mathbf{a}(x)$ , the approximated nodal value can be written as follows:

$$u(x) = \mathbf{p}^T(x) \mathbf{R}^{-1}(x) \mathbf{N}(x) u^h(x), \quad (2.4)$$

where

$$\mathbf{R}(x) = \sum_{j=1}^n w_j(x) \mathbf{p}^T(x_j) \mathbf{p}(x_j), \quad (2.5a)$$

$$\mathbf{N}(x) = [w_1(x) \mathbf{p}(x_1), w_2(x) \mathbf{p}(x_2), \dots, w_n(x) \mathbf{p}(x_n)]. \quad (2.5b)$$

Eq. (2.4) can be rewritten in the standard form as:

$$u(x) = \sum_{i=1}^n M_i^T(x) u_i(x) = \mathbf{M}^T(x) u^h(x), \quad (2.6)$$

where  $\mathbf{M}^T(x)$  indicates the MLS shape functions at point  $x$  defined as follows:

$$\mathbf{M}^T(x) = \mathbf{p}^T(x) \mathbf{R}^{-1}(x) \mathbf{N}(x). \quad (2.7)$$

### 3 Formulation of the Discrete Least-Squares Meshless (DLSM) method

The DLSM method used the strong-form solution scheme in establishing a discrete system of equations to solve linear elastic problems. For a general 2D body, as shown in Fig. 1, consider the following governing PDEs of linear elastostatic problems:

$$\begin{cases} \mu \nabla^2 u + (\lambda + \mu) \frac{\partial}{\partial x} \left( \frac{\partial u}{\partial x} + \frac{\partial v}{\partial y} \right) + f_x = 0 \\ \mu \nabla^2 v + (\lambda + \mu) \frac{\partial}{\partial y} \left( \frac{\partial u}{\partial x} + \frac{\partial v}{\partial y} \right) + f_y = 0 \end{cases} \quad \text{in } \Omega, \quad (3.1)$$

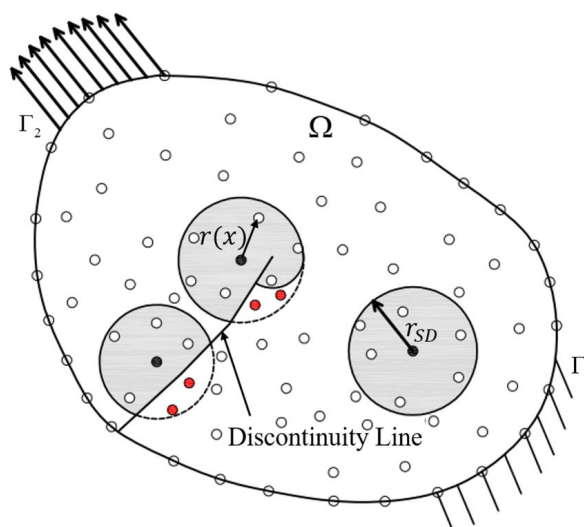


Figure 1: Domain discretization in the DLSSM method by nodal points.

with the following boundary conditions:

$$u = u^*, \quad v = v^* \quad \text{on } \Gamma_1, \quad (3.2a)$$

$$\sigma_x n_x + \tau_{xy} n_y = t_x^*, \quad \sigma_y n_y + \tau_{xy} n_x = t_y^* \quad \text{on } \Gamma_2, \quad (3.2b)$$

where  $\nabla^2$  is the 2D Laplacian operator with  $\nabla^2 = (\partial^2/\partial x^2) + (\partial^2/\partial y^2)$ ;  $\Omega$  is the solution domain containing an isotropic elastic material;  $\Gamma_1$  and  $\Gamma_2$  are the essential and natural boundaries, respectively;  $n_x$  and  $n_y$  are the outward unit normal vectors to the boundary; the components  $u^*$ ,  $v^*$  and  $t_x^*$ ,  $t_y^*$  are prescribed displacements and tractions on the boundaries  $\Gamma_1$  and  $\Gamma_2$ , respectively. The shear modulus  $\mu$  and Lamé's first parameter  $\lambda$  are defined as:

$$\mu = \frac{E}{2(1+\nu)}, \quad \lambda = \frac{E\nu}{(1-2\nu)(1+\nu)}, \quad (3.3)$$

where  $\nu$  and  $E$  are Poisson's ratio and Young's modulus, respectively. Expanding Eq. (3.1) yields:

$$\begin{cases} (\lambda+2\mu) \frac{\partial^2 u}{\partial x^2} + \mu \frac{\partial^2 u}{\partial y^2} + (\lambda+\mu) \frac{\partial^2 v}{\partial x \partial y} + f_x = 0 \\ (\lambda+2\mu) \frac{\partial^2 v}{\partial y^2} + \mu \frac{\partial^2 v}{\partial x^2} + (\lambda+\mu) \frac{\partial^2 u}{\partial x \partial y} + f_y = 0 \end{cases} \quad \text{in } \Omega, \quad (3.4)$$

Eq. (3.1) can be written in the matrix notation of the differential equation as follows:

$$\mathbf{L}(\varphi) + \mathbf{F} = 0 \quad \text{in } \Omega, \quad (3.5)$$

where  $\mathbf{F}$  denotes the external forces applied to the solution domain,  $\varphi$  is the vector of unknowns, and the second-order differential operator  $\mathbf{L}(\cdot)$  is defined as follows:

$$\mathbf{F} = [-fx - fy]^T, \quad \varphi = [uv]^T, \tag{3.6a}$$

$$\mathbf{L}(\cdot) = \mathbf{L}_1(\cdot)_{xx} + \mathbf{L}_2(\cdot)_{yy} + \mathbf{L}_3(\cdot)_{xy}, \tag{3.6b}$$

where  $\mathbf{L}_1$ ,  $\mathbf{L}_2$  and  $\mathbf{L}_3$  are defined as:

$$\mathbf{L}_1 = \begin{bmatrix} \lambda + 2\mu & 0 \\ 0 & \mu \end{bmatrix}, \quad \mathbf{L}_2 = \begin{bmatrix} \mu & 0 \\ 0 & \lambda + 2\mu \end{bmatrix}, \quad \mathbf{L}_3 = \begin{bmatrix} 0 & \lambda + \mu \\ \lambda + \mu & 0 \end{bmatrix}. \tag{3.7}$$

Additionally, the matrix form of the boundary conditions of Eqs. (3.2a) and (3.2b) can be written as follows:

$$\varphi - \varphi^* = 0 \quad \text{on } \Gamma_1, \tag{3.8a}$$

$$\mathbf{D}(\varphi) - \mathbf{t}^* = 0 \quad \text{on } \Gamma_2, \tag{3.8b}$$

where  $\varphi^*$  and  $\mathbf{t}^*$  are the components of the prescribed displacements and tractions on the boundaries  $\Gamma_1$  and  $\Gamma_2$ , respectively.  $\mathbf{D}(\varphi)$  denotes a first-order differential operator that represents the natural boundary conditions obtained by:

$$\mathbf{D}(\cdot) = \mathbf{D}_1(\cdot)_x + \mathbf{D}_2(\cdot)_y, \tag{3.9}$$

with  $\mathbf{D}_1$  and  $\mathbf{D}_2$  are defined as follow:

$$\mathbf{D}_1 = \begin{bmatrix} (\lambda + 2\mu)n_x & \mu n_y \\ \lambda n_y & \mu n_x \end{bmatrix}, \quad \mathbf{D}_2 = \begin{bmatrix} \mu n_y & \mu n_x \\ \lambda n_x & (\lambda + 2\mu)n_y \end{bmatrix}. \tag{3.10}$$

The operation of the DLSM method for solving the governing equations for all the nodes starts with the definition of residuals at a typical point  $k$  as follows:

$$R_\Omega(x_k) = \mathbf{L}(\varphi(x_k)) + \mathbf{F}(x_k) = \sum_{j=1}^N \mathbf{L}(\mathbf{M}_j(x_k)) \varphi_j + \mathbf{F}(x_k) \quad \text{in } \Omega, \quad k = 1 \approx M, \tag{3.11a}$$

$$R_1(x_k) = \varphi - \varphi^*(x_k) = \sum_{j=1}^N \mathbf{M}_j(x_k) \varphi_j - \varphi^*(x_k) \quad \text{on } \Gamma_1, \quad k = 1 \approx M_1, \tag{3.11b}$$

$$R_2(x_k) = \mathbf{D}(\varphi(x_k)) - \mathbf{t}^*(x_k) = \sum_{j=1}^N \mathbf{D}(\mathbf{M}_j(x_k)) \varphi_j - \mathbf{t}^*(x_k) \quad \text{on } \Gamma_2, \quad k = 1 \approx M_2, \tag{3.11c}$$

where  $N$  is the total number of nodes,  $M_1$  and  $M_2$  are the number of nodal points on the  $\Gamma_1$  and  $\Gamma_2$  boundaries, respectively;  $M$  is the number of nodal points in the domain;  $R_\Omega$ ,  $R_1$  and  $R_2$  are the residuals on the domain, essential and natural boundaries, respectively. The least-squares functional of residuals for the whole domain can be defined as:

$$I = \sum_{k=1}^M (R_\Omega^2(x_k)) + \alpha_1 \sum_{k=1}^{M_1} (R_1^2(x_k)) + \alpha_2 \sum_{k=1}^{M_2} (R_2^2(x_k)). \tag{3.12}$$

The penalty coefficients  $\alpha_1$  and  $\alpha_2$  are used as a convenient alternative approach to imposing and satisfying the essential and natural boundary conditions, respectively. The penalty value should be large enough to keep the coefficient matrix symmetric. Although a certain algorithm was proposed to estimate the penalty coefficients [32], the appropriate value for this coefficient is usually determined by trial and error. In this study, these coefficients are assumed to be  $\alpha_1 = 10^8$  and  $\alpha_2 = 10^4$ . By substituting Eqs. (3.11a)-(3.11c) into Eq. (3.12), the functional  $I$  is obtained as follows:

$$I = \sum_{k=1}^M \sum_{j=1}^N [\mathbf{L}(\mathbf{M}_j(x_k)) \varphi_j + \mathbf{F}(x_k)]^2 + \alpha_1 \sum_{k=1}^{M_1} \sum_{j=1}^N [\mathbf{M}_j(x_k) \varphi_j - \varphi^*(x_k)]^2 + \alpha_2 \sum_{k=1}^{M_2} \sum_{j=1}^N [\mathbf{D}(\mathbf{M}_j(x_k)) \varphi_j - \mathbf{t}^*(x_k)]^2. \quad (3.13)$$

The minimization of the functional equation (3.13) with respect to unknown parameters  $\varphi$  leads to a system of equations follows:

$$\mathbf{K}\varphi = \mathbf{F}, \quad (3.14)$$

with

$$\mathbf{K}_{ij} = \sum_{k=1}^M [\mathbf{L}(\mathbf{M}_i(x_k))]^T \mathbf{L}(\mathbf{M}_j(x_k)) + \alpha_1 \sum_{k=1}^{M_1} [\mathbf{M}_i(x_k)]^T \mathbf{M}_j(x_k) + \alpha_2 \sum_{k=1}^{M_2} [\mathbf{D}(\mathbf{M}_i(x_k))]^T \mathbf{D}(\mathbf{M}_j(x_k)), \quad (3.15a)$$

$$\mathbf{F}_i = \sum_{k=1}^M [\mathbf{L}(\mathbf{M}_i(x_k))]^T \mathbf{F}(x_k) + \alpha_1 \sum_{k=1}^{M_1} [\mathbf{M}_i(x_k)]^T \varphi^*(x_k) + \alpha_2 \sum_{k=1}^{M_2} [\mathbf{D}(\mathbf{M}_i(x_k))]^T \mathbf{t}^*(x_k), \quad (3.15b)$$

where  $\mathbf{M}_i$  is the MLS shape function of node  $i$ . The final stiffness matrix  $\mathbf{K}$  in Eq. (3.14) is in the symmetric banded form. Therefore, an efficient iterative method can be used to provide solutions to the system of equations. The solution to Eq. (3.14) yields the value of unknown nodal parameters.

## 4 Definition of strong discontinuities

Belytschko et al. [16] noted that for numerical modeling of cracks, the dependent variables such as displacements must be discontinuous at all points on the crack surface, similar to nonconvex boundaries. Accordingly, the conventional DLSM method must undergo certain modifications as it employs highly smooth shape functions. In this paper, the visibility criterion, diffraction, and transparency approaches are employed to modify the influence domain and weight function of nodal points near the crack surface, especially at the crack tip.

#### 4.1 Discontinuous weight function by the visibility criterion

The visibility criterion [16] is the simplest and most straightforward method for defining discontinuities in the meshless method introduced to simulate strong discontinuities in the EFG method. The method has implemented discontinuities in the support domain; thus, the weight function will also be discontinuous.

In this method, the line of discontinuity is considered to be opaque like a wall. Consider node I in Fig. 2 as a light source with a light range  $r_{SD}$ . The influence domain of node I will be  $\Omega_I$  if the discontinuity is not defined. By definition, the crack is a discontinuity in the body, and the emitted ray from the point I intersects the wall (the discontinuity line). Therefore, the points previously located in influence domain I behind the wall to be in the shadow will be consequently excluded from the support domain of node I. Fig. 2 shows the modified support domain  $\Omega_I^{VIS}$  of node I in the vicinity of the crack tip. Despite the simplicity and accuracy of the visibility criterion to define discontinuities such as cracks, this approach has some limitations in dealing with nonconvex boundaries [7].

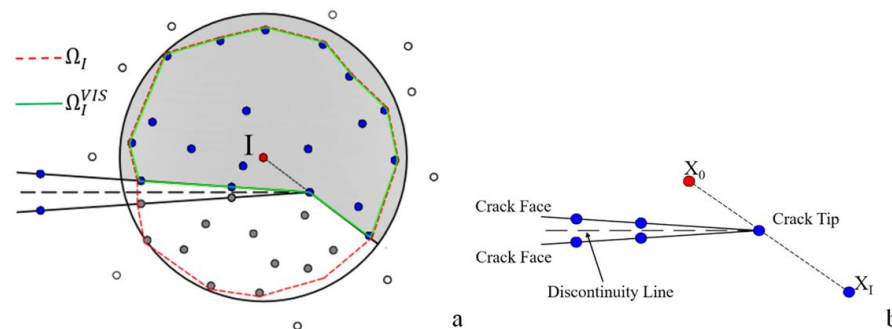


Figure 2: (a) the gray points are removed from the support domain of node I in the vicinity of the crack tip in the visibility criterion approach; (b) the performance of the visibility criterion at the crack tip.

#### 4.2 Modification of the weight function by the diffraction approach

Organ et al. [9] described the diffraction approach, an improved version of the visibility criterion approach for constructing the shape function in the crack tip region. This approach is inspired by the diffraction of light in objects. In this approach, similar to the visibility criterion, the discontinuity line is considered to be opaque. However, the rays emitted from node I are diffracted at the crack tip, so some of the points removed in the visibility criterion using the diffraction approach can fall within the influence domain of node I. The diffraction weight parameters highly differ from the equations used to construct the support domain and weight functions [7].

According to Fig. 3, when the light ray emitted from node I to point  $x$  intercepts with the discontinuity line, the weight function is modified using the weight parameter as

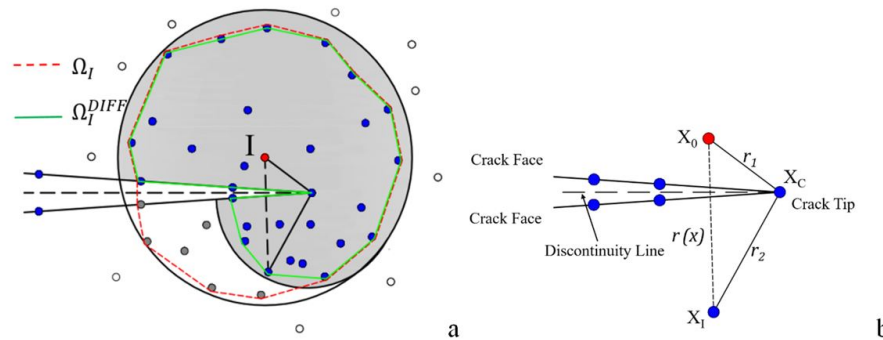


Figure 3: a) Modification of the influence domain in the diffraction approach; b) the weight parameters of the diffraction approach.

follows:

$$r_I(x) = \left( \frac{r_1 + r_2(x)}{r(x)} \right)^\zeta r(x), \quad (4.1)$$

where  $r_2(x) = |X_I - X_C|$ ,  $r_1 = |X_C - X_0|$  and  $r(x) = |X_I - X_0|$ . As a result, by choosing a larger index  $\zeta$  in Eq. (4.1), the modified weight function decreases sharply at the opposite side of the crack. Therefore, the value of the weight function behind the crack is somehow discontinuous compared to the crack front. The exponent  $\zeta$  is used to reduce the size of the support domain behind the crack. Suitable choices for  $\zeta$  values 1 and 2 were proposed in [9]. In the present study, the best results are obtained by  $\zeta = 2$ . Fig. 3(a) shows the original  $\Omega_I$  and modified  $\Omega_I^{DIFF}$  diffraction domain of node I.

### 4.3 Treatment of the weight function in the transparency approach

In the transparency approach [9], the crack line is defined by a function with varying degrees of transparency. In this case, the discontinuity line at the crack tip is assumed completely transparent. By moving away from the crack tip along the discontinuity line, the degree of transparency is reduced. Consider the point of intersection of the  $X_I - X_0$  line with the discontinuity line in Fig. 4, the longitudinal parameter of the weight function in the transparency approach can be modified as follows [15]:

$$r_I(x) = r(x) + \rho_I \left( \frac{r_C(x)}{\bar{r}_C} \right)^\zeta, \quad \zeta \geq 2, \quad (4.2)$$

where  $r(x) = |X_I - X_0|$ ;  $\rho_I$  denotes the dilatation parameter of node I, and  $r_C(x)$  is the size of the line segment between the crack tip and the intersection point. As shown in Fig. 4,  $\bar{r}_C$  represents the intersection distance, where the segment of the discontinuity line is considered opaque. The exponent  $\zeta$  is a free value proposed in [9] assumed to be

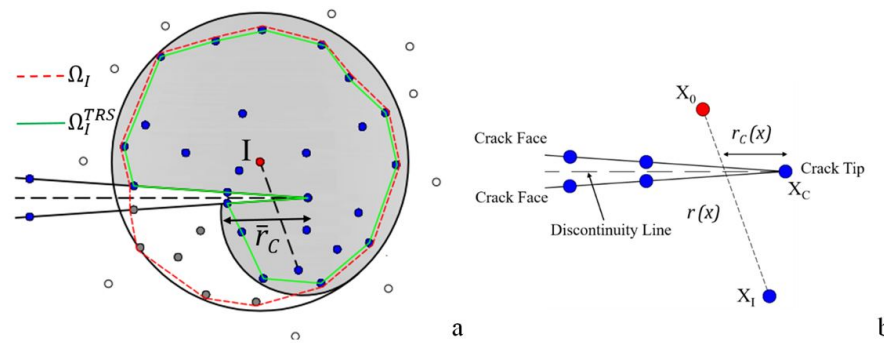


Figure 4: a) Original  $\Omega_I$  and modified  $\Omega_I^{TRS}$  support domain by the transparency approach; b) the performance of the transparency approach near the crack tip.

$\zeta \geq 2$ , which is considered to be  $\zeta = 3$  in this study. In this approach, due to a small angle between the line  $X_I - X_C$  and the discontinuity line for nodes directly adjacent to the discontinuity, the weight function has a steep gradient along the line ahead of the notch tip. To overcome this problem, all nodal points must have a minimum distance from the crack surface. According to research [9], this distance must be considered larger than  $\gamma h$ , where  $h$  is the average nodal spacing and  $0 < \gamma < 1$ , in which  $\gamma = 0.25$  is usually assumed. It was easier to apply transparency to 3D problems than to the diffraction approach [7]. The treatment of the support domain of node I in the transparency approach is shown by  $\Omega_I^{TRS}$  in Fig. 4(a).

## 5 Determination of SIFs in LEFM

In this study, linear elastic fracture mechanics (LEFM) approaches are used to examine linearly elastic materials. In the LEFM, the stress field contains crack-tip singularity despite the small external loads. Irwin [37] proposed the Stress Intensity Factor (SIF),  $\mathbf{K}$ , to describe the stress and displacement fields in the crack tip region [38]. This concept is based on the decomposition of the crack configuration into three different types of deformation: opening mode, shearing mode, and tearing mode, respectively referred to as Mode-I, Mode-II, and Mode-III of fracture deformations, respectively. The stress fields near the crack tip for a general case of mixed mode (Mode-I/II) loading along a single direction are given in matrix form as [39]:

$$\sigma = \left( \frac{1}{\sqrt{2\pi r}} \right) \mathbf{f}_\theta^{I,II} \mathbf{K}, \quad (5.1)$$

where

$$\sigma = \begin{bmatrix} \sigma_1 \\ \sigma_2 \\ \sigma_{12} \end{bmatrix}, \quad (5.2a)$$

$$\mathbf{f}_\theta^{I,II} = \begin{bmatrix} \cos\left(\frac{\theta}{2}\right) \left(1 - \sin\left(\frac{\theta}{2}\right) \sin\left(\frac{3\theta}{2}\right)\right) & -\sin\left(\frac{\theta}{2}\right) \left(2 + \cos\left(\frac{\theta}{2}\right) \cos\left(\frac{3\theta}{2}\right)\right) \\ \cos\left(\frac{\theta}{2}\right) \left(1 + \sin\left(\frac{\theta}{2}\right) \sin\left(\frac{3\theta}{2}\right)\right) & \sin\left(\frac{\theta}{2}\right) \cos\left(\frac{\theta}{2}\right) \cos\left(\frac{3\theta}{2}\right) \\ \cos\left(\frac{\theta}{2}\right) \sin\left(\frac{\theta}{2}\right) \cos\left(\frac{3\theta}{2}\right) & \cos\left(\frac{\theta}{2}\right) \left(1 - \sin\left(\frac{\theta}{2}\right) \sin\left(\frac{3\theta}{2}\right)\right) \end{bmatrix}, \quad (5.2b)$$

$$\mathbf{K} = \begin{bmatrix} K_I \\ K_{II} \end{bmatrix}, \quad (5.2c)$$

where  $K_I$  and  $K_{II}$  are the SIF values. The radial distance  $r$  from the crack tip to the selected point, the angle  $\theta$  between  $r$  and the discontinuity line ahead of the crack, and the local coordinate system  $x'_1, x'_2$  are shown in Fig. 5.

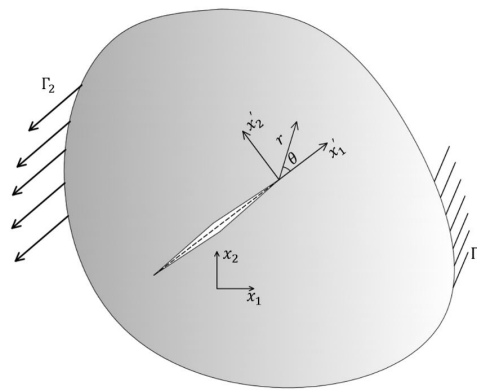


Figure 5: The polar system at the crack tip in a homogeneous material.

The (SIF)  $\mathbf{K}$  is the most important parameter for analyzing fracture problems and cracked structures. The local and global schemes have been proposed in numerical methods for evaluating the SIFs. The local scheme is based on the displacements or stresses in the crack tip region, such as stress or displacement extrapolation. The global scheme is based on measuring energy release rates such as Interaction Integral and  $J$ -integral [40]. In this study, the stress extrapolation and the  $J$ -integral methods are employed to evaluate Mode-I SIF.

### 5.1 Stress Extrapolation Method (SEM)

The stress at any nodal point can be measured by simulating the cracked body after employing the approaches to defining discontinuities in the DLSSM method. Therefore,  $K_I$

and  $K_{II}$  can be calculated by stress components of any point using Eq. (5.1). The relationship between the stress near the crack tip and  $K_I$  is defined as:

$$K_I = \sigma(r, \theta) \sqrt{2\pi r}. \quad (5.3)$$

The above term is valid as  $r$  approaches zero and can be adjusted to compute the Mode-I SIF. However, this condition is inappropriate since the result is unreliable after  $r$  has approached zero in numerical methods [21]. In this method, a tangent extrapolation of the curve of  $K_I$  values obtained from stress at many points with a distance  $r$  from the crack tip is used to calculate  $K_I$ . In this study, to obtain more accurate results, the distance  $r$  from the crack tip to the selected points used to calculate the SIFs ranges from  $a/15$  to  $a/4$ , where  $a$  is the half length of the center crack and the crack length for the edge-cracked plate.

## 5.2 $J$ -integral method

The  $J$ -integral provides a generalization of the relationship between the SIFs and the energy release rate, which is defined as:

$$J = \int_{\Gamma} \left[ W(\varepsilon_{ij}) dx_2 - T_i \frac{\partial U_i}{\partial x_1} dS \right], \quad (5.4)$$

where  $\Gamma$  a contour in a counterclockwise direction around the crack tip,

$$W(\varepsilon_{ij}) = \int_0^{\varepsilon} \sigma_{ij} d\varepsilon_{ij}$$

is strain energy density, where  $\sigma_{ij}$  and  $\varepsilon_{ij}$  represent stress and strain tensors, respectively. Besides,  $dS$  is the length increment along the contour  $\Gamma$  and  $U_i$  is the displacement vector component.  $T_i$  is the traction vector component at any point on the  $\Gamma$  given as:

$$T_i = \sigma_{ij} n_j, \quad (5.5)$$

where  $n_j$  is the outward unit normal vector to contour  $\Gamma$ . This integral is path-independent, equal to the nonlinear energy release rate and uniquely characterizes stresses and strains at the crack tip. Using the concept of energy release rate, the relationship between  $J$ ,  $K_I$ , and  $K_{II}$  SIFs is defined as follows [41]:

$$J = \frac{1}{\bar{E}} (K_I^2 + K_{II}^2), \quad (5.6)$$

where  $\bar{E} = E/(1 - \nu^2)$  for plane strain,  $\bar{E} = E$  for plane stress, and  $E$  is Young's modulus.

## 6 Numerical examples

In this section, the accuracy and efficiency of the DLSM method are assessed by employing different approaches to defining discontinuities, namely, the visibility criterion, diffraction, and transparency approaches, to analyze fracture problems. For this purpose, three numerical examples of 2D problems are investigated using an irregular mesh of nodes. Furthermore, isotropic linear elastic materials and plane stress conditions are assumed in all problems. In the numerical example, the problem domain was discretized by three different irregular nodal distributions. In this study, the global error and convergence rate are defined by the error norm as follows:

$$e^K = \frac{\sqrt{\sum_{i=1}^n (K_i^{exact} - K_i^{num})^2}}{\sqrt{\sum_{i=1}^n (K_i^{exact})^2}}, \quad (6.1)$$

where  $e^K$  is the error norm for the SIFs,  $K_i^{exact}$  is the available analytical solution for the SIFs, and  $K_i^{num}$  is the SIFs obtained from the numerical solution of the DLSM method, and  $n$  is the number of nodal points used for calculating the error norm.

### 6.1 An edge crack problem

The first numerical example presents an edge-cracked plate under a distributed constant load. The uniform tensile loading applied  $\sigma = 1\text{Pa}$  and  $L = 16\text{cm}$ ,  $W = 8\text{cm}$ , and  $a = 3.2\text{cm}$  are the geometrical configurations of the cracked plate, as shown in Fig. 6. The material model is linear elastic with the following properties: The Young's modulus is  $E = 1000\text{Pa}$ , and the Poisson ratio is  $\nu = 0.3$ .

The problem is simulated using three different irregular nodal distributions, with 623, 1084, and 2088 nodes listed as coarse, mild, and fine distributions, respectively, for domain discretization. The analytical Mode-I SIF  $K_I$  for the edge-cracked plate is defined as:

$$K_I = f\left(\frac{a}{W}\right) \sigma \sqrt{\pi a}, \quad (6.2)$$

where  $\sigma$  is the applied tractions,  $a$  is the crack length, and geometry function  $f\left(\frac{a}{W}\right)$  is a dimensionless value given by [42]:

$$f\left(\frac{a}{W}\right) = 1.12 - 0.231\left(\frac{a}{W}\right) + 10.55\left(\frac{a}{W}\right)^2 - 21.72\left(\frac{a}{W}\right)^3 + 30.39\left(\frac{a}{W}\right)^4, \quad (6.3)$$

where  $a$  and  $W$  are the crack length and the width of the loaded plate, respectively. The  $J$ -integral and SEM approaches are adopted to determine the SIF  $K_I$ . Table 1 compares the  $K_I$  results of the numerical  $J$ -integral on the circular integration path of radius  $R = 0.4\text{cm}$  and SEM for different approaches to defining discontinuities with three nodal distributions with the exact solution. The results indicated the high accuracy and efficiency of the

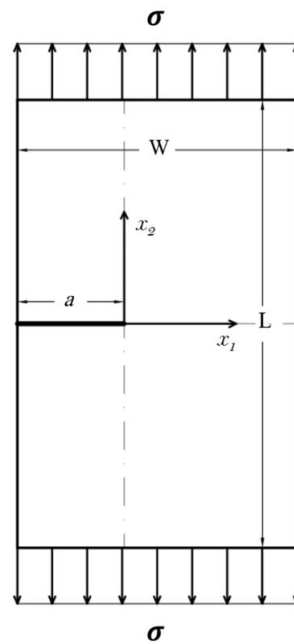


Figure 6: An edge crack problem under a distributed constant load.

DLSM method in simulating this fracture problem. Besides, Table 1 demonstrates that the diffraction approach has relatively outperformed other approaches, and the higher accuracy of the SIFs can be obtained by the  $J$ -integral approach.

Although the  $J$ -integral method is path independent, according to the existing approximations, five circular paths with various radii are considered to investigate the radius size effect on determining the  $K_I$  values from the  $J$ -integral method. Table 2 shows the error of the  $J$ -integral SIF values for the three approaches to defining discontinuities in fine nodal distributions. Comparing the results demonstrated that the paths with larger radii have lower accuracy. Despite the slight difference in error between the three studied methods, the highest accuracy was obtained using the diffraction approach.

The stress  $\sigma_{22}$  in front of the notch tip along the crack line is presented in Fig. 7. The

Table 1: The comparison of different methods of calculating the SIFs in terms of the global error for different approaches to defining discontinuities with three nodal distributions in edge crack problem.

Approach	SIF Method	623 nodes		1084 nodes		2088 nodes		Exact
		$K_I(\text{pa}\cdot\text{cm}^{1/2})$	Error(%)	$K_I(\text{pa}\cdot\text{cm}^{1/2})$	Error(%)	$K_I(\text{pa}\cdot\text{cm}^{1/2})$	Error(%)	
Visibility criterion	SEM $J$ -integral	4.9376	8.204	5.1889	3.533	5.4416	1.164	503790
		5.0603	5.925	5.2920	1.616	5.4134	0.640	
Diffraction	SEM $J$ -integral	5.0151	6.764	5.2096	3.148	5.4360	1.060	503790
		5.1163	4.884	5.3015	1.439	5.4101	0.579	
Transparency	SEM $J$ -integral	4.9929	7.177	5.2019	3.291	5.4382	1.101	503790
		5.1002	5.182	5.2980	1.505	5.4115	0.604	

Table 2: The comparison of different approaches to defining discontinuities in terms of the  $K_I$  error for various paths.

Approach	$J$ (Path 1)	$J$ (Path 2)	$J$ (Path 3)	$J$ (Path 4)	$J$ (Path 5)
	$R = 0.2\text{cm}$	$R = 0.4\text{cm}$	$R = 0.8\text{cm}$	$R = 1.2\text{cm}$	$R = 1.6\text{cm}$
	Error%	Error%	Error%	Error%	Error%
Visibility criterion	1.593	0.640	0.668	1.586	3.366
Diffraction	0.060	0.579	0.141	1.069	2.855
Transparency	0.774	0.604	0.176	1.078	2.113

contour plot of the stress components of the diffraction approach computed by fine nodal distributions and the enlarged region in the vicinity of the crack tip is presented in Fig. 8. It shows the stress concentration at the tip of the crack.

The convergence rate of the present method obtained by the SEM error values is depicted in Fig. 9, demonstrating its stability and convergence characteristics for employing the different approaches to defining discontinuities. The comparison of the results indicates the effectiveness of the accuracy of numerical methods in increasing the number of nodes used to discretize the domain. However, considering the slope of the convergence lines shown in Fig. 9, the visibility criterion is relatively more sensitive to this change.

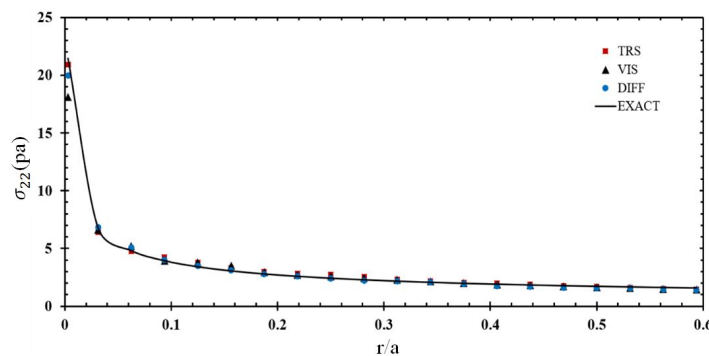


Figure 7: The normal stress  $\sigma_{22}$  along the discontinuity line ( $x_2=0$ ); Exact (EXACT), visibility criterion (VIS), diffraction approach (DIFF) and transparency approach (TRS).

## 6.2 A central crack problem under uniform traction

In this example, a plate with a center crack of length  $2a = 1.6\text{cm}$ , and dimensions of  $2W = 4\text{cm}$ , and  $L = 8\text{cm}$ , under uniform traction of  $\sigma = 3\text{Pa}$  in the  $x_2$  direction is considered as shown in Fig. 10. The elasticity parameters of the plate are  $E = 30\text{KPa}$  and  $\nu = 0.25$ . The example is simulated under plane stress conditions.

The analytical solution for the SIF in this problem is given by Eq. (6.2) with the fol-

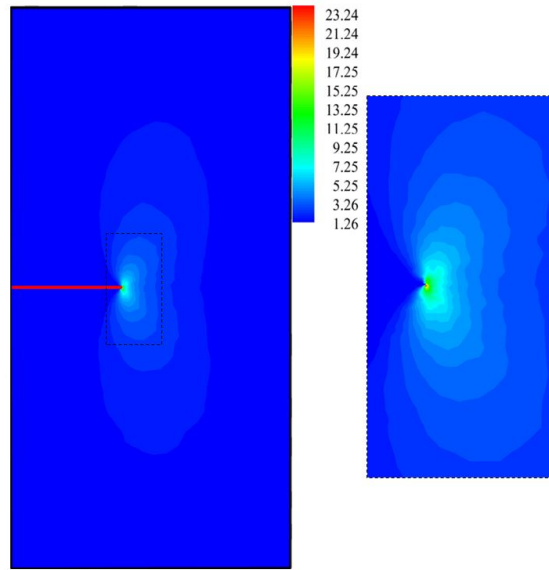


Figure 8: Contour plot of  $\sigma_{22}$  for an edge crack problem by the diffraction approach.

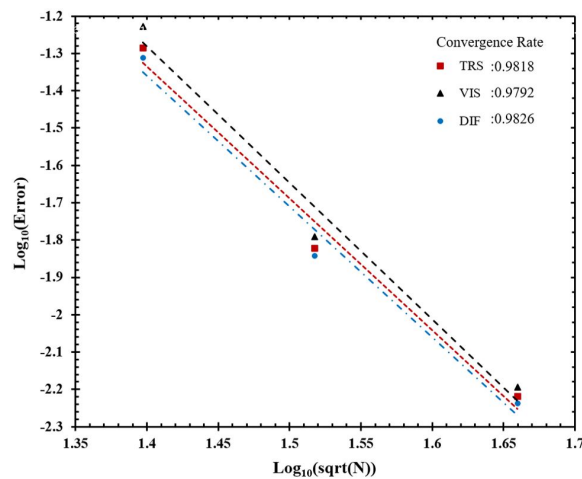


Figure 9: Convergence rate of the three approaches to defining discontinuities (first example); visibility criterion (VIS), diffraction approach (DIF), and transparency approach (TRS).

lowing geometry correction factor [43]:

$$f\left(\frac{a}{W}\right) = \sqrt{\sec\left(\frac{\pi a}{2W}\right)} \left[1 - 0.025\left(\frac{a}{W}\right)^2 + 0.06\left(\frac{a}{W}\right)^4\right], \quad (6.4)$$

where  $a$  and  $W$  are half of the crack length and half of the infinite plate width, respec-

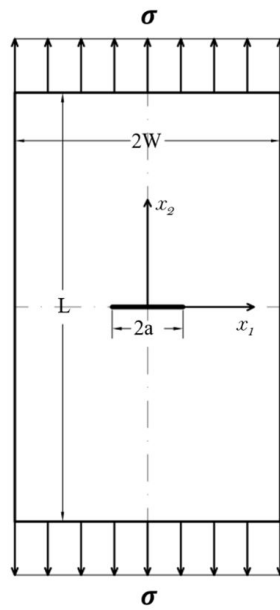


Figure 10: Geometric model of a central crack problem under uniform traction.

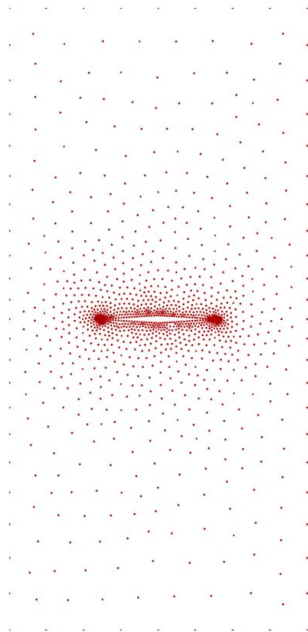


Figure 11: A discrete model of a center-cracked plate produced by irregularly distributed nodes.

Table 3: Normalized  $K_I$  SIFs for different approaches to defining discontinuities with three nodal distributions in the center crack problem.

Approach	628 nodes		1289 nodes		2648 nodes	
	$K_I / K_{exact}$	Error%	$K_I / K_{exact}$	Error%	$K_I / K_{exact}$	Error%
Visibility criterion	0.9394	6.059	0.9796	2.039	1.0118	1.179
Diffraction	0.9536	4.644	0.9813	1.866	1.0094	0.941
Transparency	0.9480	5.196	0.9809	1.908	1.0105	1.047

tively. The problem is simulated using 628,1289 and 2648 irregularly distributed nodes with increased node densities in the vicinity of the crack tip, as shown in Fig. 11.

The contour plot of  $\sigma_{22}$  stress obtained by the DLSM method using 2648 irregularly distributed nodes for different approaches to defining discontinuities and the enlarged region is depicted in Fig. 12. As can be seen, all three methods can capture the stress singularity at the crack tip well.

The numerical results of the normalized  $K_I$  SIF values obtained by the  $J$ -integral method on the circular contour of radius  $R = 0.2\text{cm}$  and the error values for three weight function modification techniques are presented in Table 3. All these error values are small, implying the high accuracy of this meshless method. Moreover, as was the case in the previous example, the global error is reduced in fine nodal distribution. According to this table, it can be concluded again that the diffraction approach has outperformed the visibility criterion and transparency approaches. Fig. 13 shows a good convergence rate obtained by three approaches to defining discontinuities in the DLSM method.

Furthermore, in this example, five circular contours around the crack tip are intended for the integration path to calculate the SIF using the  $J$ -integral method to investigate the

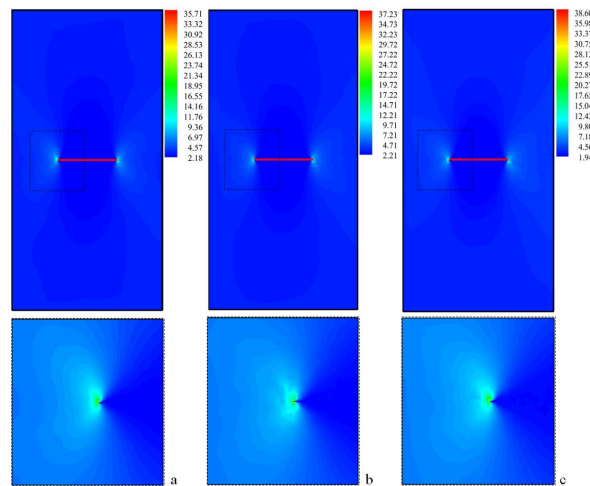


Figure 12: Contour plot of  $\sigma_{22}$  for a center-cracked plate by 2648 nodal distributions. a) visibility criterion; b) diffraction approach; c) transparency approach.

Table 4: The error values of the  $K_I$  SIFs for the three approaches to defining discontinuities on paths with different radii.

Approach	$J$ (Path 1)	$J$ (Path 2)	$J$ (Path 3)	$J$ (Path 4)	$J$ (Path 5)
	$R=0.1\text{cm}$	$R=0.2\text{cm}$	$R=0.4\text{cm}$	$R=0.6\text{cm}$	$R=0.8\text{cm}$
	Error%	Error%	Error%	Error%	Error%
Visibility criterion	4.604	1.179	1.016	1.682	2.931
Diffraction	4.415	0.941	0.331	1.167	2.220
Transparency	4.431	1.047	0.382	1.213	2.354

sensitivity to the integration path. Table 4 presents the  $K_I$  error values calculated by the  $J$ -integral method on different paths in the fine nodal point distribution. As can be seen, the two middle paths, the paths with radius  $R = 0.2\text{cm}$  and  $R = 0.4\text{cm}$  have the lowest error rate, while on the path very close to the crack tip, the error values increase at once, and the least error was recorded using the diffraction approach.

### 6.3 A slant crack problem

The third example investigates the problem of a square plate with a center slant crack under uniform tension of  $\sigma = 1\text{Pa}$  in the  $x_1$  direction, as shown in Fig. 14. The geometrical parameters  $W = 3\text{cm}$ ,  $a = 0.6\text{cm}$ ,  $\beta = 45^\circ$  (see Fig. 14), and the properties of the material  $E = 200\text{Gpa}$ ,  $\nu = 0.3$  are considered for the numerical simulation of this example. Three nodal distributions with 3615, 1831, and 791 nodes are explored for numerical computation by the DLSSM method. The mild nodal distribution is shown in Fig. 15. Furthermore, this problem is modeled by the FEM scheme as one of the most popular numerical simulation schemes by modeling this domain in the ABAQUS software package with 23047 quad

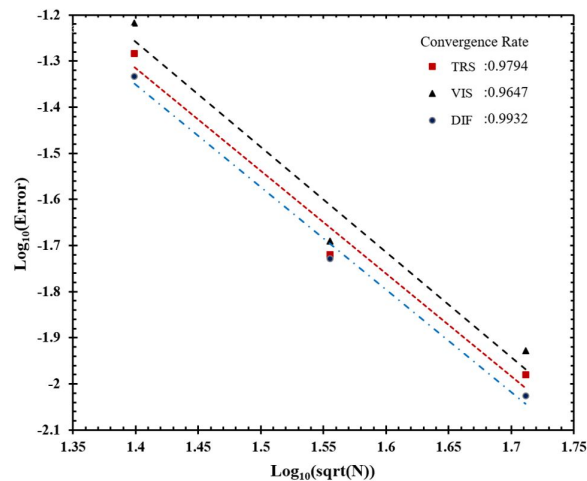


Figure 13: Convergence rate of three approaches to defining discontinuities (second example); visibility criterion (VIS), diffraction approach (DIF), and transparency approach (TRS).

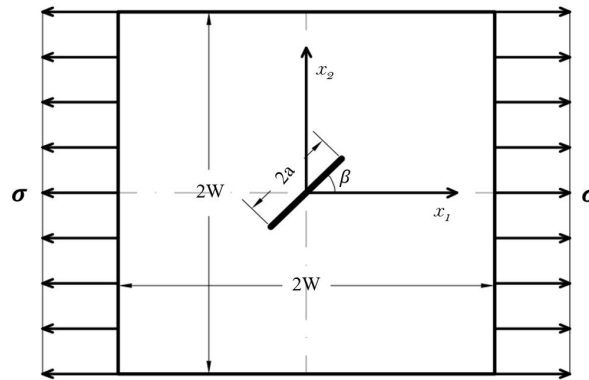


Figure 14: A center slant crack problem under uniform tension.

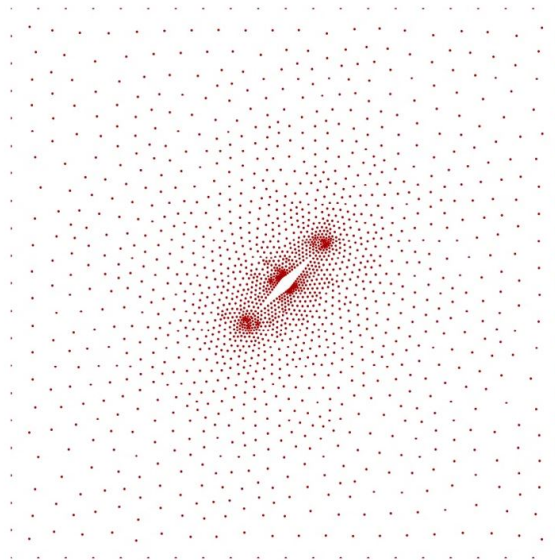


Figure 15: Discretization of a center slant-cracked plate.

meshes.

The contour plot of the stress  $\sigma_{11}$  for the DLSSM method using the diffraction approach with fine nodal distributions and the FEM are depicted in Fig. 16. The stress densities due to the singularity fields near the crack tip are clearly visible in these images. A comparison of the  $\sigma_{11}$  results obtained from the DLSSM method in front of the crack tip along the direction  $\theta = 0^\circ$ ,  $x_1 = x_2$  for the different approaches to defining discontinuities in three nodal distributions and those obtained by the FEM with an ultra-fine mesh is demonstrated in Fig. 17. The numerical  $\sigma_{11}$  curves of the DLSSM are well overlapped with these

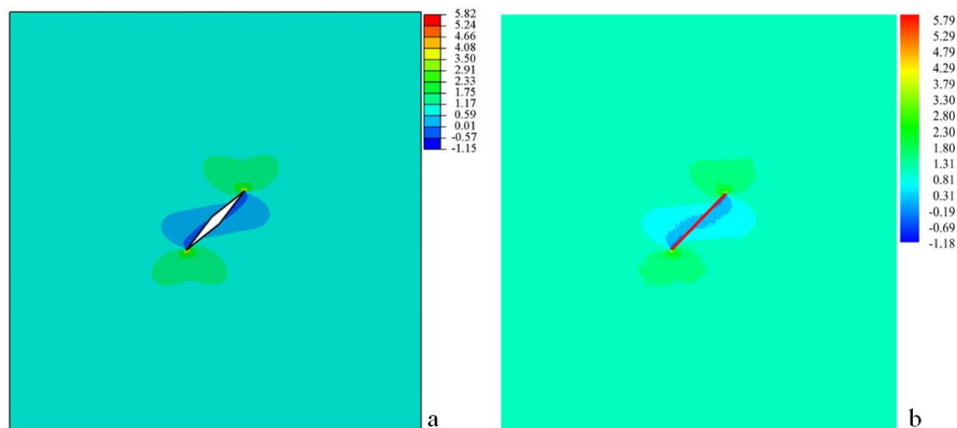


Figure 16: Contour plot of  $\sigma_{11}$  for the center slant-cracked plate; a) the FEM scheme by the ABAQUS software with fine meshes; b) the DLSM method by the diffraction approach with the discretization of 3615 nodes.

FEM results for the center slant crack problem with  $\beta = 45^\circ$ , which again verifies the accuracy and effectiveness of the DLSM method for crack problems. However, the comparison of the curves shows a relatively better overlapping of the diffraction approach with the results obtained from the FEM than the other two approaches. Besides, significant changes in the accuracy rate are observed by reducing the number of nodal points.

## 7 Conclusions

Firstly, the DLSM method was applied in this paper to solve the crack problems in isotropic materials. Three numerical examples were simulated to investigate the accuracy and effectiveness of the proposed method using different nodal distributions. The problems were discretized irregularly by increasing the number of nodal points in the vicinity of the crack tip due to the stress singularity at this field. Because of using high-continuity shape functions in this method, some modifications were required in the influence domain near the crack surface. The visibility criterion, diffraction, and transparency approaches were employed in this study to define discontinuities in weight functions. The path-independent  $J$ -integral and stress extrapolation methods were applied to determine the SIFs, with the  $J$ -integral presenting a higher degree of accuracy. It was shown that the diffraction approach had outperformed the transparency and visibility criterion approaches in dealing with discontinuous boundaries. It was also demonstrated that the visibility criterion was relatively more sensitive to the reduced number of nodal points than the other approaches. Although the visibility criterion approach can be easily used to simulate discontinuities, this sensitivity can be mainly attributed to reducing the num-

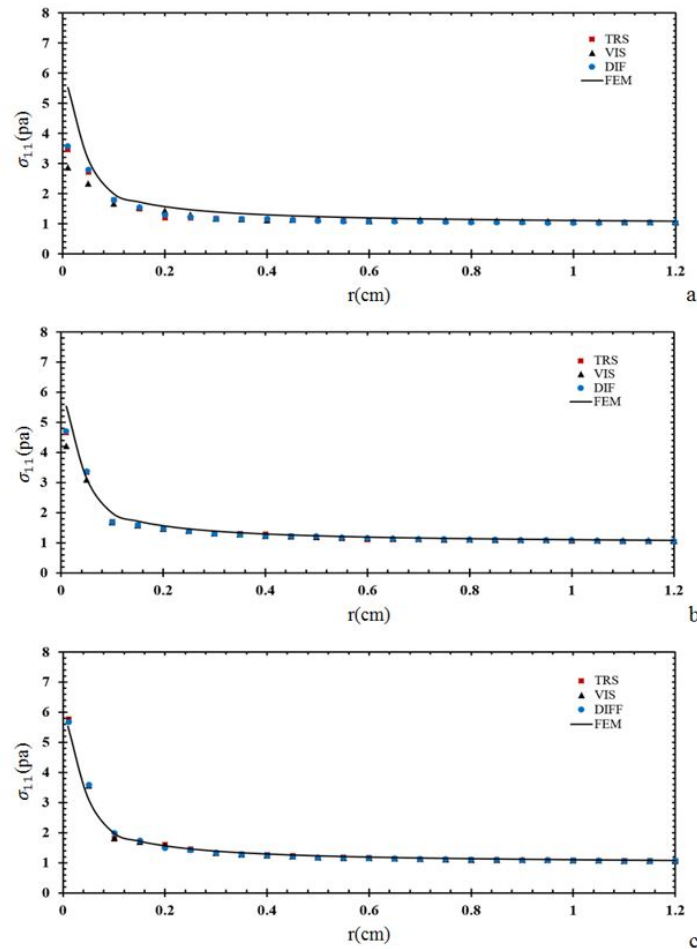


Figure 17: The normal stress  $\sigma_{11}$  along the discontinuity line for  $\beta=45^\circ$  and  $\theta=0^\circ$ , a) 791 nodes, b) 1831 nodes, c) 3615 nodes; FEM (FEM), visibility criterion (VIS), diffraction approach (DIF) and transparency approach (TRS).

ber of nodes in the influence domain of the master node near the crack tip.

Several circular paths were considered as integration paths to study the effects of the existing approximations on the SIF values obtained from the  $J$ -integral method. Although the effects of the radius of the integration path on the error values cannot be exactly determined, it can be generally and cautiously stated that intermediate paths had shown higher accuracy.

The comparison of the results and the errors and the high convergence rate in the studied numerical examples pointed to the effectiveness and efficiency of the DLSSM method in using different approaches to defining discontinuities for solving the fracture mechanics problems.

## References

- [1] G. R. LIU, *Mesh Free Methods*, 1st ed, Boca Raton: CRC Press, 2003.
- [2] G. H. QIN, AND S. W. YU, *Fracture and damage analysis of a cracked body by a new boundary element model*, *Commun. Numer. Methods Eng.*, 13 (1997), pp. 327–336.
- [3] T. BELYTSCHKO, AND T. BLACK, *Elastic crack growth in finite elements with minimal remeshing*, *Int. J. Numer. Methods Eng.*, 45(5) (1999), pp. 601–620.
- [4] H. JIA, Y. NIE, AND J. LI, *XFEM for fracture analysis in 2D anisotropic elasticity*, *Adv. Appl. Math. Mech.*, 9(1) (2017), pp. 125–143.
- [5] S. R. BEISSEL, G. R. JOHNSON, AND C. H. POPELAR, *An element-failure algorithm for dynamic crack propagation in general directions*, *Eng. Fract. Mech.*, 61(3-4) (1998), pp. 407–425.
- [6] P. O. BOUCHARD, F. BAY, AND Y. CHASTEL, *Numerical modelling of crack propagation: automatic remeshing and comparison of different criteria*, *Comput. Methods Appl. Mech. Eng.*, 192(35-36) (2003), pp. 3887–3908.
- [7] V. P. NGUYEN, T. RABCZUK, S. BORDAS, AND M. DUFLOT, *Meshless methods: A review and computer implementation aspects*, *Math. Comput. Simulat.*, 79 (2008), pp. 763–813.
- [8] T. BELYTSCHKO, Y. KRONGAUZ, M. FLEMING, D. ORGAN, AND W. K. LIU, *Smoothing and accelerated computations in the element-free Galerkin method*, *J. Comput. Appl. Math.*, 74 (1996), pp. 111–126.
- [9] D. ORGAN, M. FLEMING, T. TERRY, AND T. BELYTSCHKO, *Continuous meshless approximations for nonconvex bodies by diffraction and transparency*, *Comput. Mech.*, 18 (1996), pp. 225–235.
- [10] M. FLEMING, Y. A. CHU, B. MORAN, AND T. BELYTSCHKO, *Enriched element-free Galerkin methods for crack tip fields*, *Int. J. Numer. Methods Eng.*, 40 (1997), pp. 1483–1504.
- [11] T. RABCZUK, AND T. BELYTSCHKO, *Cracking particles: a simplified meshfree method for arbitrary evolving cracks*, *Int. J. Numer. Methods Eng.*, 61(13) (2004), pp. 2316–2343.
- [12] T. RABCZUK, AND G. ZI, *A meshfree method based on the local partition of unity for cohesive cracks*, *Comput. Mech.*, 39(6) (2007), pp. 743–760.
- [13] A. CARPINTERI, *Post-peak and post-bifurcation analysis of cohesive crack propagation*, *Eng. Fract. Mech.*, 32 (1989), pp. 265–278.
- [14] A. CARPINTERI, *A scale-invariant cohesive crack model for quasi-brittle materials*, *Eng. Fract. Mech.*, 69 (2002), pp. 207–217.
- [15] T. P. FRIES, AND H. G. MATTHIES, *Classification and Overview of Meshfree Methods*, Brunswick: Informatikbericht, Technical University Braunschweig, 2003.
- [16] T. BELYTSCHKO, L. GU, AND Y. Y. LU, *Fracture and crack growth by element-free Galerkin methods*, *Model. Simul. Mater. Sci. Eng.*, 2 (1994), pp. 519–534.
- [17] B. MURAVIN, AND E. TURKEL, *Spiral weight for modeling cracks in meshless numerical methods*, *Comput. Mech.*, 38 (2006), pp. 101–111.
- [18] H. PIRALI, F. DJAVANROODI, AND M. HAGHPANAHI, *Combined visibility and surrounding triangles method for simulation of crack discontinuities in meshless methods*, *J. Appl. Math.*, 2012 (2012), 715613.
- [19] M. KHEZRI, M. ABBASI, AND K. J. R. RASMUSSEN, *A combined meshfree/finite strip method for analysis of plates with perforations and cracks*, *Thin Wall Struct.*, 111 (2017), pp. 113–125.
- [20] W. MA, G. LIU, AND H. MA, *A smoothed enriched meshfree Galerkin method with two-level nesting triangular sub-domains for stress intensity factors at crack tips*, *Theory Appl. Fract. Mech.*, 101 (2019), pp. 279–293.
- [21] J. LEI, Y. XU, Y. GU, AND M. FAN, *The generalized finite difference method for in-plane crack*

- problems, *Eng. Anal. Bound. Elem.*, 98 (2019), pp. 147–156.
- [22] W. YAO, X. ZHOU, AND F. BERTO, *Continuous smoothed particle hydrodynamics for cracked nonconvex bodies by diffraction criterion*, *Theory Appl. Fract. Mech*, 108 (2020), 102584.
- [23] M. H. AFSHAR, AND H. ARZANI, *Solving Poisson's equations by the discrete least squares meshless method*, *WIT Trans. Model. Simulat.*, 42 (2006), pp. 23–31.
- [24] A. R. FIROOZJAEI, AND M. H. AFSHAR, *Discrete least squares meshless method with sampling points for the solution of elliptic partial differential equations*, *Eng. Anal. Bound. Elem.*, 33 (2009), pp. 83–92.
- [25] M. H. AFSHAR, AND A. R. FIROOZJAEI, *Adaptive simulation of two dimensional hyperbolic problems by collocated discrete least squares meshless method*, *Comput. Fluids*, 39 (2010), pp. 461–470.
- [26] A. R. FIROOZJAEI, AND M. H. AFSHAR, *Discrete Least Squares Meshless (DLSM) method for simulation of steady state shallow water flows*, *Scientia Iranica*, 18(4) (2011), pp. 835–845.
- [27] G. SHOBEYRI, AND M. H. AFSHAR, *Simulating free surface problems using discrete least squares meshless method*, *Comput. Fluids*, 39 (2010), pp. 461–470.
- [28] G. SHOBEYRI, AND M. H. AFSHAR, *Adaptive simulation of free surface flows with discrete least squares meshless (DLSM) method using a posteriori error estimator*, *Eng. Comput.*, 29(8) (2012), pp. 794–813.
- [29] M. H. AFSHAR, J. AMANI, AND M. NAISIPOUR, *A node enrichment adaptive refinement in Discrete Least Squares Meshless method for solution of elasticity problems*, *Eng. Anal. Bound. Elem.*, 36 (2012), pp. 385–393.
- [30] M. H. AFSHAR, M. NAISIPOUR, AND J. AMANI, *Node moving adaptive refinement strategy for planar elasticity problems using discrete least squares meshless method*, *Finite Elem. Anal. Des.*, 47 (2011), pp. 1315–1325.
- [31] J. AMANI, M. H. AFSHAR, AND M. NAISIPOUR, *Mixed discrete least squares meshless method for planar elasticity problems using regular and irregular nodal distributions*, *Eng. Anal. Bound. Elem.*, 36 (2012), pp. 894–902.
- [32] S. FARAJI, M. KOLAHDOOZAN, AND M. H. AFSHAR, *Mixed discrete least squares meshless method for solving the linear and nonlinear propagation problems*, *Scientia Iranica*, 25 (2) (2018), pp. 565–578.
- [33] S. NIKRAVESH, AND M. H. AFSHAR, *An adaptive node regeneration technique for the efficient solution of elasticity problems using MDLSM method*, *Eng. Anal. Bound. Elem.*, 50 (2015), pp. 198–211.
- [34] S. NIKRAVESH, M. H. AFSHAR, AND S. FARAJI, *RPIM and RPIM-MLS-based MDLSM method for the solution to elasticity problems*, *Scientia Iranica*, 23 (6) (2016), pp. 2458–2468.
- [35] Z. JANNESARI, AND M. TATARI, *A Meshfree Technique for Numerical Simulation of Reaction-Diffusion Systems in Developmental Biology*, *Adv. Appl. Math. Mech.*, 9 (2017), pp. 1225–1249.
- [36] S. N. ATLURI, H. T. LIU, AND Z. D. HAN, *Meshless local Petrov-Galerkin (MLPG) mixed collocation method for elasticity problems*, *CMES Comput. Model Eng.*, 14 (2006), pp. 141–152.
- [37] G. R. IRWIN, *Analysis of stresses and strains near the end of a crack traversing a plate*, *J. Appl. Mech. T. ASME*, 24 (1956), pp. 361–364.
- [38] A. AGHAHOSEINI, A. KHOSRAVIFARD, AND T. Q. BUI, *Efficient analysis of dynamic fracture mechanics in various media by a novel meshfree approach*, *Theory Appl. Fract. Mec.*, 99 (2018), pp. 161–176.
- [39] R. ZHANG, AND R. GUO, *Determination of crack tip stress intensity factors by singular Voronoi cell finite element model*, *Eng. Fract. Mech.*, 197 (2018), pp. 206–216.
- [40] S. D. DAXINI, AND J. M. PRAJAPATI, *A review on recent contribution of meshfree methods to*

- structure and fracture mechanics applications*, Sci. World J., 2014 (2014), 247172.
- [41] N. T. NGUYEN, T. Q. BUI, CH. ZHANG, AND T. T. TRUONG, *Crack growth modeling in elastic solids by the extended meshfree Galerkin radial point interpolation method*, Eng. Anal. Bound. Elem., 44 (2014), pp. 87–97.
- [42] X. ZHUANG, Y. CAI, AND CH. AUGARDE, *A meshless sub-region radial point interpolation method for accurate calculation of crack tip fields*, Theory Appl. Fract. Mec., 69 (2014), pp. 118–125.
- [43] T. L. ANDERSON, *Fracture Mechanics: Fundamentals and Applications*, 4st ed. Boca Raton: CRC Press, 2017.